Materials Today 97 (2026) 103352

Contents lists available at ScienceDirect

Materials Today

journal homepage: www.elsevier.com/locate/mattod

Membrane-fusogenic polyamidoamines mediate ultralow-dose mRNA transfection through direct cytosolic delivery

Xiaofei Zhao [a,1], Qiongzhe Ren [a,1], Xin Wang [a], Siyu Wang [a], Congcong Xu [b], Zhiyuan Zhong [a,b,*], Chao Deng [a,*]

[a] Biomedical Polymers Laboratory, and Jiangsu Key Laboratory of Advanced Functional Polymer Materials, College of Chemistry, Chemical Engineering and Materials Science, and State Key Laboratory of Radiation Medicine and Protection, Soochow University, Suzhou 215123, China
[b] College of Pharmaceutical Sciences, Soochow University, Suzhou 215123, China

ARTICLE INFO

Keywords:
mRNA therapeutics
Fusogenic polyamidoamines
Low-dose transfection
Pancreas-specific transfection
Cancer immunotherapy

ABSTRACT

mRNA therapeutics represent a revolutionary strategy for treating diverse diseases, yet their efficacy and clinical translation encounter critical challenges in achieving efficient cytosolic mRNA delivery. Here, we report that membrane-fusogenic polyamidoamines (PAA_{mef}) mediate high-efficacy mRNA transfection by directly delivering mRNA to cytosol. Synthesized through a Ugi four-component reaction, PAA_{mef} packs mRNA into virus-mimicking nanoparticles that enter cytosol via membrane fusion, while enabling swift mRNA release through reduction-triggered polymer degradation. This unique trafficking pathway renders PAA_{mef} exceptional transfection efficiency across diverse cell types including challenging immune cells at ultralow doses of 0.1–0.2 pg mRNA/cell, matching viral vector efficiency. The intraperitoneal administration of mRNA-Luc@PAA_{mef} at an exceptionally low dose of 0.25 μg mRNA/mouse achieves pancreas-specific transfection with approximately 90% selectivity, potently suppressing orthotopic KPC pancreatic tumors through delivering IL-12 mRNA. PAA_{mef} with direct cytosolic mRNA delivery opens a new horizon for mRNA therapy.

Introduction

mRNA therapeutics represent a revolutionary strategy for disease prevention and treatment, yet their efficacy and clinical translation encounter critical challenges in achieving efficient cytosolic mRNA delivery, primarily due to a cascade of extracellular and intracellular obstacles [1–4]. The development of advanced delivery systems with enhanced safety and efficiency constitutes a crucial prerequisite for realizing the potential of mRNA therapeutics [5–7]. While viral vectors exhibit superior transfection capabilities, their clinical application is restricted by significant immunogenicity risks, potential genomic integration hazards, and complicated manufacturing processes [8,9]. Non-viral vectors have gained prominence as safer and more scalable solutions, and offered improved biocompatibility and reduced immune jeopardy [10–13]. Nevertheless, current non-viral delivery platforms demonstrate limited transfection efficiency, with inadequate stability in physiological environments, inefficient endosomal escape, and suboptimal intracellular release serving as the critical biological barriers [14–16].

Non-viral delivery systems predominantly rely on endosomal pathway to enter cells, yet even state-of-the-art lipid nanoparticles (LNPs) achieve merely 1–4% of RNA payloads to the cytosol [16–19]. To enhance endosomal escape efficiency, high doses of carriers are frequently required to induce endosomal disruption, which paradoxically heightens toxicity concerns while compromising therapeutic effectiveness [20–22]. Furthermore, endosome rupture usually triggers inflammatory responses via binding cytosolic galectins with sugars on inner endosomal membrane, thereby engendering adverse side effects [23,24]. Therefore, there is an imperative need to engineer mRNA vectors capable of achieving efficient low-dose cytosolic delivery to advance clinical applications.

In this contribution, we have designed a library of polyamidoamines (PAAs) that can effectively transfect mRNA at ultralow doses (Fig. 1). PAAs are synthesized via Ugi four-component reaction, which is characterized by mild reaction conditions, high-throughput synthesis, and simultaneous incorporation of multiple functional groups (ionizable

* Corresponding authors.
E-mail addresses: zyzhong@suda.edu.cn (Z. Zhong), cdeng@suda.edu.cn (C. Deng).
[1] These authors contributed equally.

https://doi.org/10.1016/j.mattod.2026.103352
Received 7 July 2025; Received in revised form 27 March 2026; Accepted 14 April 2026
Available online 22 April 2026

amine, lipid, disulfide bonds, etc.), facilitating comprehensive investigation of structure-delivery relationships. Best performing PAA (P1114) can interact with the cell membrane through membrane fusion and directly deliver mRNA into the cytosol. We hypothesize that the optimized PAA (PAA_{mef}) mediates membrane fusion-driven cytosolic mRNA delivery through a three-stage process: (i) rapid electrostatic adsorption of positively charged mRNA@PAA_{mef} nanocomplexes onto cell membrane; (ii) lipid–mediated fusion of nanocomplexes with cell membrane, and (iii) glutathione-triggered mRNA release in the cytosol. mRNA@PAA_{mef} nanocomplexes demonstrate exceptional transfection performance across diverse cell types (immune cells, cancer cells, and healthy cells) at ultralow doses (0.1–0.2 pg mRNA/cell), achieving efficiency comparable to viral vectors, and maintain efficacy even in 80% serum-containing medium. Intraperitoneal administration of mRNA@PAA_{mef} at an exceptionally low dose of 0.25 μg mRNA/mouse affords efficient pancreatic transfection coupled with high selectivity up to 90%, which is further verified by significant inhibition of orthotopic KPC pancreatic cancer through delivering IL-12 mRNA.

Results

Rational design and screening of PAAs for mRNA delivery

The Ugi multicomponent reaction is one of the most versatile reactions and has been sophisticatedly utilized in the synthesis of polymers and lipids [25–28]. We developed a combinatorial library of polyamidoamines (PAAs) (denoted as PABCD) via a one-pot Ugi four-component reaction under mild conditions. By systematically varying 2 different dicarboxylic acids (A), 3 different isocyanides (B), 5 different diamines (C), and 5 different aliphatic aldehydes (D), we synthesized and characterized 76 structurally distinct PAAs. A1 bearing disulfide bonds was prioritized for initial screening due to its glutathione-responsive cleavage capacity, which facilitates intracellular mRNA release while mitigating the potential toxicity of cationic polymers [29,30]. For mRNA delivery evaluation, PAAs were complexed with EGFP mRNA (mGFP) via simple vortex mixing and then applied to HeLa cells (Fig. 2**a**). Quantitative analysis using flow cytometry revealed significant variations in transfection efficiency, as measured by GFP-

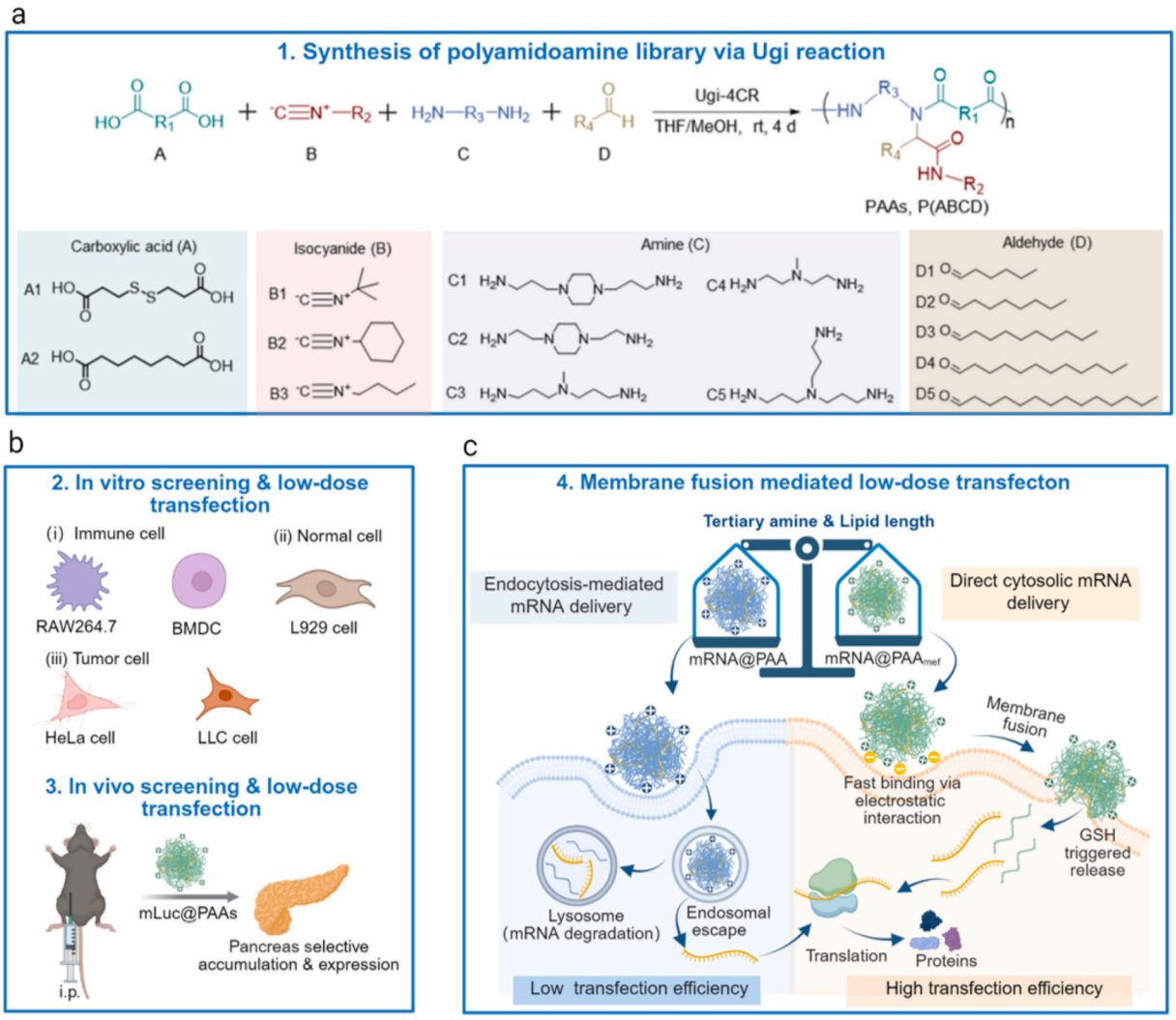

Fig. 1. Design and screening scheme of polyamidoamines (PAAs) for mRNA delivery. (a) Synthesis of PAAs (denoted as PABCD, where A-D represent dicarboxylic acids, isocyanides, diamines, and aldehydes, respectively) via Ugi four-component reaction and chemical structures of the four components used in the synthesis of PAAs library. (b) In vitro screening of PAAs and analysis of the relationship between activity and structure, with the optimal formulations achieving low-dose and efficient transfection of immune cells, normal cells, and tumor cells. In vivo screening of representative PAAs for low-dose and highly selective pancreas transfection. (c) The optimized PAAs (PAA_{mef}) mediates membrane fusion-driven cytosolic mRNA delivery through the follow steps: (i) rapid electrostatic adsorption of positively charged mRNA@PAA_{mef} nanocomplexes onto cell membrane; (ii) lipid-mediated fusion of nanocomplexes with cell membrane; and (iii) glutathione-triggered mRNA release in the cytosol.

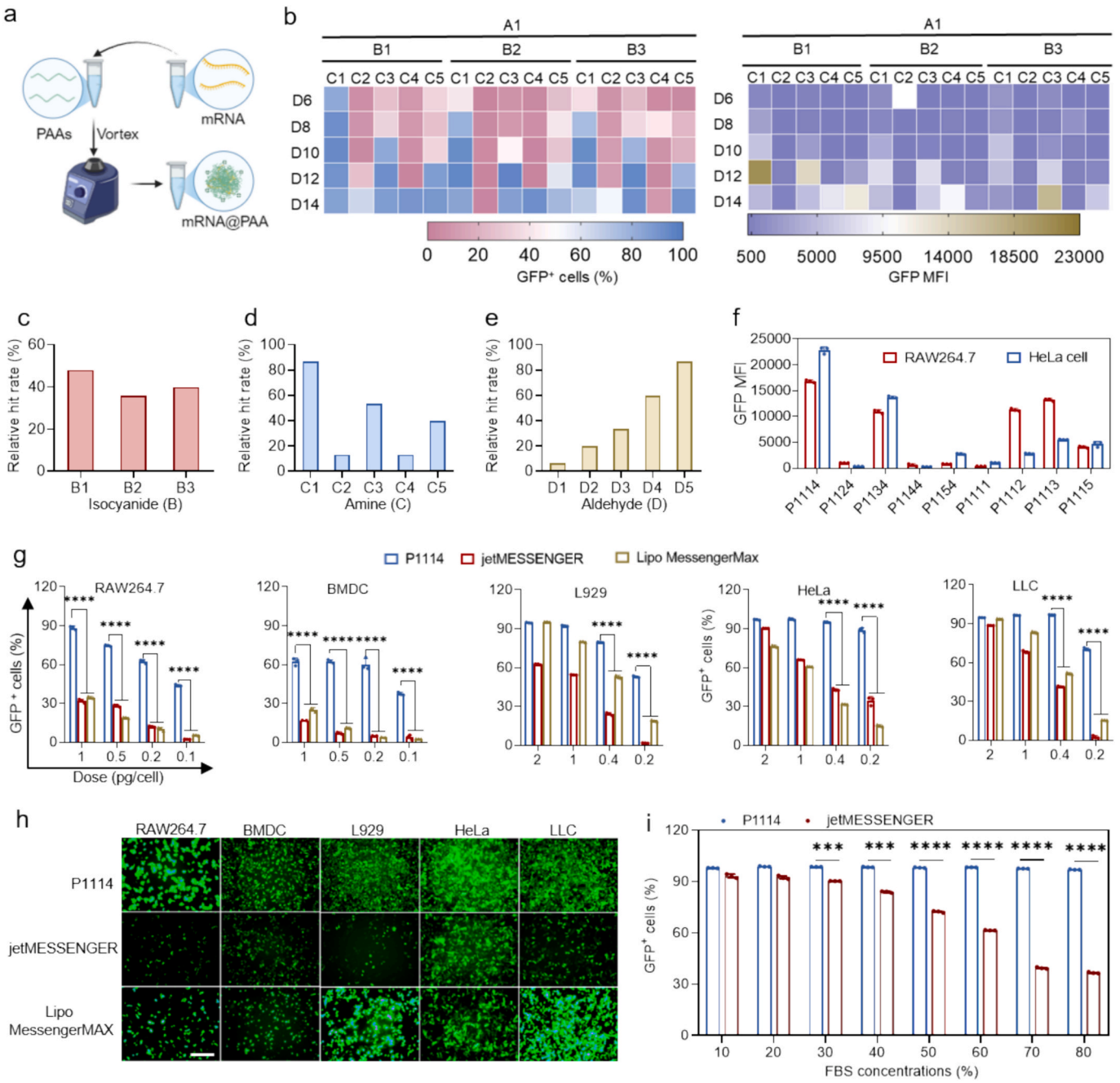

Fig. 2. Screening and structure–activity relationship study of PAAs for mRNA delivery. (a) Preparation of mRNA@PAAs nanocomplexes via vortex mixing of PAAs with mRNA. (b) High-throughput screening of the PAAs library. The GFP expression in HeLa cells, following treatment with mGFP@PAAs for 24 h, is depicted in a heat map (mGFP concentration: 0.25 μg/mL, n = 3). (c-e) Effect of isocyanides (c), diamines (d), and aldehydes (e) on mRNA delivery efficacy, as quantified by relative hit rate (% GFP^+ cells ≥ 50%). (f) Transfection efficiency of representative PAAs (P11C4 and P111D) in HeLa and RAW264.7 cells (mGFP: 0.25 μg/mL, n = 3). (g) Transfection efficiency of mGFP@P1114 in comparison to positive controls Lipo MessengerMax and jetMESSENGER in immune cells (RAW264.7 and BMDC), normal cells (fibroblasts L929 cells), and tumor cells (HeLa and LLC cells), following treatment with varying doses of mGFP for 24 h (n = 3). (h) Fluorescence imaging of immune cells (RAW264.7 and BMDC cells, 0.5 pg mRNA/cell), fibroblasts L929 cells (0.4 pg mRNA/cell), and tumor cells (HeLa and LLC cells, 0.4 pg mRNA/cell). Scale bar: 200 μm. (i) Transfection efficiency of HeLa cells treated with mGFP@P1114 and mGFP@jetMESSENGER for 24 h in the medium containing 10–80% FBS (0.5 μg/mL), n = 3. All values are expressed as mean ± s.d. For (g) and (i), statistical significance was determined using ordinary one-way ANOVA with multiple comparisons. *$p < 0.05$; **$p < 0.01$; ***$p < 0.001$; ****$p < 0.0001$; ns, not significant.

positive cell percentages and mean fluorescence intensity (MFI) (Fig. 2**b**). Fig. 2**c** showed that isocyanides bearing linear, branched, and cyclic alkyl groups displayed comparable transfection efficiency. Diamines bearing tertiary amines spaced by three carbons from primary amines (C1, C3) outperformed those with two-carbon spacers (C2, C4), and linear diamines (C1, C3) surpassed branched analogues (C5) (Fig. 2**d**). For aliphatic aldehyde, the transfection efficiency correlated positively with aliphatic chain length (Fig. 2**e**). Among all variants, P1114 demonstrated superior performance with the highest GFP-positive rate and MFI. The control P2114 polymer lacking disulfide bonds exhibited reduced efficiency mainly owing to the slow and incomplete mRNA release under cytosol-mimicking reductive environments (Fig. S1). The GSH-triggered degradation of P1114 polymer was verified by a pronounced reduction in the molecular weight, leading to

rapid nanocomplex disassembly and over 70% mRNA release within 12 h (Fig. S2). Based on the structure–activity relationship analysis, we further selected representative PAAs (P11C1 and P111D) to evaluate the transfection of macrophage. Similar trends were observed in RAW264.7 macrophages, with P1114 demonstrating the top performance (Fig. 2**f**). Additionally, All PAAs exhibited good cytocompatibility in HeLa cells with a cell viability of above 80% (Fig. S3). We proceeded to fine-tune the mass ratios of P1114 to mRNA (w/w), and found that even at low ratio of 5/1 afforded excellent transfection efficiency (90%), which could be promoted to 95% upon increasing the ratio to 20/1 (Fig. S4). Therefore, the P1114/mRNA at a mass ratio of 20/1 was adopted in subsequent studies.

Non-viral vectors generally exhibit dose-dependent transfection efficiency, typically affording deficient protein expression below 1.0 pg mRNA/cell due to their limited endosomal escape capability [31,32]. Systematic evaluation of mRNA@P1114 performance across diverse cell types revealed exceptional transfection capabilities, particularly in notoriously hard-to-transfect immune cells (Fig. 2**g**). Of note, mGFP@P1114 induced robust protein expression in RAW264.7 macrophages and BMDCs at doses of 0.1–1.0 pg mRNA/cell. At a low dose of 0.1 pg mRNA/cell, P1114 conferred 40% GFP^+ BMDCs and 50% GFP^+ RAW264.7 cells, representing 18 ~ 22 fold enhancement over commercial transfection reagents (LipoMessengerMAX and jetMESSENGER). The platform demonstrated versatile applicability, achieving 70% ~ 90% transfection in tumor cells and around 55% in normal cells at 0.2 pg mRNA/cell, significantly outperforming benchmark reagents. Notably, P1114 revealed 4 ~ 26 fold increase in transfection efficiency compared to FDA-approved ALC-0315 formulation across all tested cell lines at low mRNA doses (0.1–0.4 pg/cell) and also significant superiority over SM-102 LNP formulation under identical experimental conditions (Fig. S5). In contrast, GFP expression levels in the mLuc@P1114 group were equivalence to those observed in the PBS control (Fig. S6), confirming that the high transfection efficiency of mGFP@P1114 was specifically due to GFP mRNA delivery rather than non-specific vector effects. Confocal imaging further revealed that robust GFP expression across cell types at low mRNA doses (Fig. 2**h**). Additionally, mRNA@P1114 exhibited good cytocompatibility with cell viability remaining above 90% across multiple cell lines (Fig. S7). Nanoparticle tracking analysis (NTA) revealed that one pg mRNA corresponded to 5500 mRNA@P1114 nanocomplexes (Fig. S8), suggesting that one cell was transfected by about 550 nanoparticles at 0.1 pg mRNA/cell. The efficiency approaches levels comparable to viral performance, as evidenced by particle-to-plaque forming unit (P/PFU) ratios of approximately 10–1000 for natural viruses [33,34]. Notably, P1114 nanocomplexes maintained transfection competence in biological matrices, achieving 95% transfection efficiency in HeLa in media containing 80% fetal bovine serum (FBS) versus 35% for jetMESSENGER (Fig. 2**i**). This serum tolerance addresses a critical challenge for cationic polymer vectors, which typically suffer from protein interference in physiological environments [35–37].

Membrane fusion-mediated low-dose mRNA transfection

The structure–activity relationship analysis revealed that tertiary amines and lipids significantly influence mRNA delivery efficiency, prompting us to evaluate the physicochemical properties of representative PAAs (P11C4 and P111D) and nanocomplexes. The structure of P11C4 and P111D was verified by the distinct resonance signals in ^1H NMR spectra corresponding to characteristic protons from dicarboxylic acids, isocyanides, diamines, and aliphatic aldehydes (Fig. S9 and S10). Gel permeation chromatography (GPC) analysis revealed that P11C4 and P111D exhibited molecular weights of 1.5–2.5 kDa (Table S1). Through the strong interactions between mRNA and PAAs, both P11C4 and P111D afforded high encapsulation efficiencies exceeding 85% (Fig. S11). Zeta potential of P11C4 nanocomplexes varied from + 10 to + 25 mV, correlating with the type of ionizable amines (Fig. 3**a**). In contrast, P111D nanocomplexes maintained surface charges between + 16 mV and + 30 mV. Dynamic light scattering (DLS) measurement revealed that P11C4 nanocomplexes exhibited hydrodynamic diameters spanning from 90 to 235 nm, with particle sizes showing an inverse correlation with zeta potential, suggesting electrostatic interactions served as a critical driving force for mRNA condensation. Meanwhile, P111D formulations presented small sizes between 90 and 140 nm, owing to enhanced hydrophobic interactions from extended alphatic chains. The resulting nanocomplexes displayed monodisperse spherical nanoparticles as revealed by AFM and TEM measurements (Fig. 3**b and** Fig. S12**).** Furthermore, mRNA@P1114 nanocomplexes exhibited exceptional stability in neutral and acidic buffers, maintaining consistent particle sizes for up to 30 days (Fig. S13a). In PBS and 80% FBS media, significant particle aggregation was observed mainly due to salt-induced charge screening effects and serum protein adsorption (Fig. S13b, c).

The successful delivery of mRNA necessitates overcoming critical intracellular and extracellular barriers, especially cellular internalization and endosomal escape [38,39]. To elucidate the structure–activity relationship, we initially assessed the cellular uptake profiles of P11C4- and P111D-based nanocomplexes in HeLa cells. The results reveal that the ionizable amine groups significantly affect the uptake efficiency of P11C4 nanocomplexes, with P1114 and P1134 showing the highest uptake efficiency (Fig. 3**c**). Conversely, P111D nanocomplexes maintain similar uptake across aldehyde variants (except P1115), likely due to their shared positive charge. Despite the limited impact on cellular uptake, aliphatic aldehydes were found to substantially influence transfection efficiency in P111D formulations (Fig. 2**f**), promoting mechanistic investigation of intracellular trafficking pathways. Various endocytosis inhibitors including amiloride, chlorpromazine, dynasore, and methylated β-cyclodextrins were employed to reveal the endocytosis pathway. Dynasore treatment significantly reduced P1111 and P1112 uptake to 64.5% and 77.8%, respectively (Fig. 3**d**), indicating a primary role of dynamin-dependent endocytosis. In contrast, P1113, P1114 and P1115 nanocomplexes displayed inhibitor-resistant uptake, consistent with membrane fusion-mediated internalization as reported previously [23,40]. Fluorescence resonance energy transfer (FRET) analysis confirmed the fusion between P111D and HeLa cells, with fusion efficiency increasing progressively with lipid length, reaching a maximum of approximately 85.2% for P1114 (Fig. 3**e-g**). Following gold nanoparticle labeling, Au/mRNA@P1114 showing comparable sizes and morphology to the original one demonstrated direct cytoplasmic delivery via membrane fusion as revealed by Bio-TEM analysis (Fig. S14). Nevertheless, Au/mRNA@P1111 exhibited noticeable endosomal localization, confirming its reliance on endocytosis pathways for cellular entry. Real-time tracking of mLuc-Cy5@P1114 internalization revealed that red fluorescence signals (mLuc-Cy5@P1114) colocalized with the green fluorescence signals (cell membrane) within 5 min, with colocalization progressively increasing over time (Fig. 3**h**). By 30 min, a portion of the red signal entered the cytosols, suggesting that mLuc-Cy5@P1114 rapidly adsorbed onto the cell membrane via electrostatic interactions and subsequently entered cytosols. To investigate mRNA release, we monitored the dissociation process of mLuc-Cy5 and $P1114^{FITC}$ after treatment with mLuc-Cy5@$P1114^{FITC}$ at different time points (Fig. 3**i**). The results exhibited that the majority of red fluorescence signals (mLuc-Cy5) overlapped with green ones ($P1114^{FITC}$), forming yellowish puncta at 30 min. Over time, the red and green signals gradually separated and converged inside the cells, suggesting that $P1114^{FITC}$ effectively dissociated from mLuc-Cy5 and promoted the translocation of mRNA into the cytosols. Concurrently, the lack of significant colocalization between mLuc-Cy5 and the nucleus suggests that the mRNA is predominantly distributed in the cytosols (Fig. S15). CLSM images reveal divergent endosomal entrapment pattern. P1111 and P1112 formulations presented significant colocalization with endosomes, as evidenced by the overlay of red fluorescence signals (mLuc-Cy5) with green fluorescence signals (endosomes), appearing as yellow

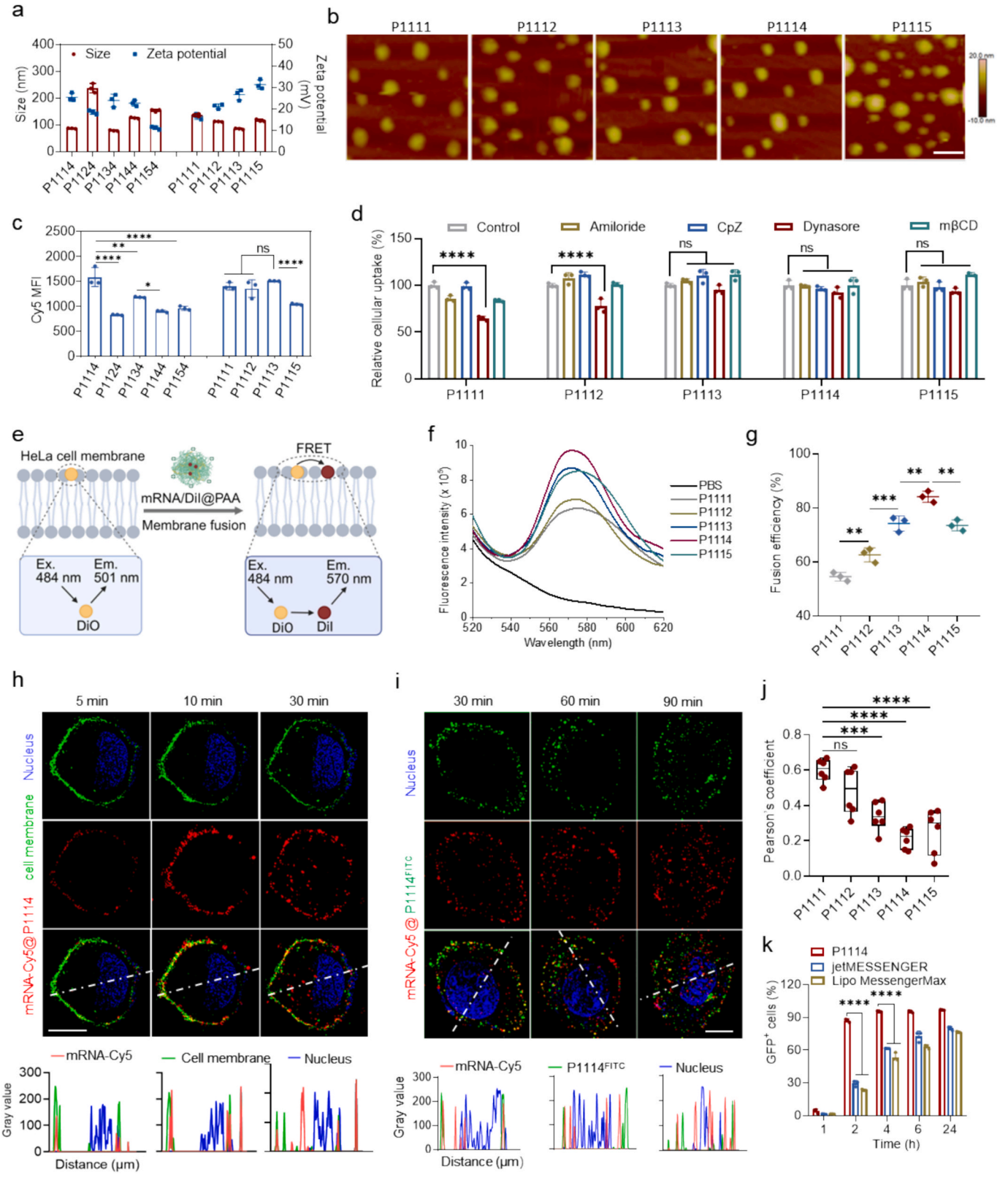

(caption on next page)

Fig. 3. Membrane fusion-mediated efficient mRNA transfection. (a) The size and zeta potential of representative mGFP@PAAs nanocomplexes formed from representative PAAs (n = 3). (b) Representative AFM image of mGFP@PAAs. Scale bar, 200 nm. (c) Cellular uptake of mLuc-Cy5@PAAs in Hela cells after treated for 2 h (mLuc-Cy5: 0.5 μg/mL, n = 3). (d) Relative cellular uptake of mLuc-Cy5@PAAs in HeLa cells in the presence of different endocytosis inhibitors including amiloride (AM, macropinocytosis-mediated endocytosis inhibitor), chlorpromazine (CPZ, clathrin-mediated endocytosis inhibitor), dynasore (dynamin-mediated endocytosis inhibitor), and methylated β-cyclodextrins (mβCD, caveolae-mediated endocytosis inhibitor) (n = 3). (e) Schematic illustration for monitoring membrane fusion between HeLa cells and mRNA/DiI@PAAs via FRET assay. (f) The intensity of the emission wavelength of the fluorescent donor DiO (Em, 495–505 nm) and the fluorescent acceptor DiI (Em, 540–620 nm) at an excitation wavelength of 484 nm. (g) The fusion efficiency between HeLa cells and mRNA/DiI@PAAs (n = 3). (h) Snapshots of mLuc-Cy5@P1114 entry into HeLa cells at different time points captured by high intelligent and sensitive structured illumination microscope (HIS-SIM). The nuclei were stained with Hoechst (blue), the cell membranes were stained with wheat germ agglutin (WGA-FITC) (green), and mLuc-Cy5@PAAs were shown in red. Scale bar, 10 μm. (i) CLSM images of the dissociation of the dually labeled nanocomplex mLuc-Cy5@P1114FITC in HeLa cells at different time points. Scale bar, 10 μm (j) Endosomal escape of representative nanocomplexes in HeLa cells were quantified by Pearson's correlation coefficient (Pearson's R value) between endosomes and mLuc-Cy5 (n = 6). (k) The expression of GFP in HeLa cells at different time points (mGFP: 0.5 μg/mL, n = 3). All values are expressed as mean ± s.d. For (c), (d), (g), (j), and (k), statistical significance was determined using ordinary one-way ANOVA with multiple comparisons. *$p < 0.05$; **$p < 0.01$; ***$p < 0.001$; ****$p < 0.0001$; ns, not significant.

puncta (Fig. S16). In contrast, P1113, P1114, and P1115 exhibited minimal endosomal colocalization. Quantitative analysis using Pearson's coefficients further revealed a gradual reduction in lysosomal colocalization as the lipid chain length increased, with P1114 and P1115 showing the least colocalization (Fig. 3j), signifying an endosomal bypass mechanism.

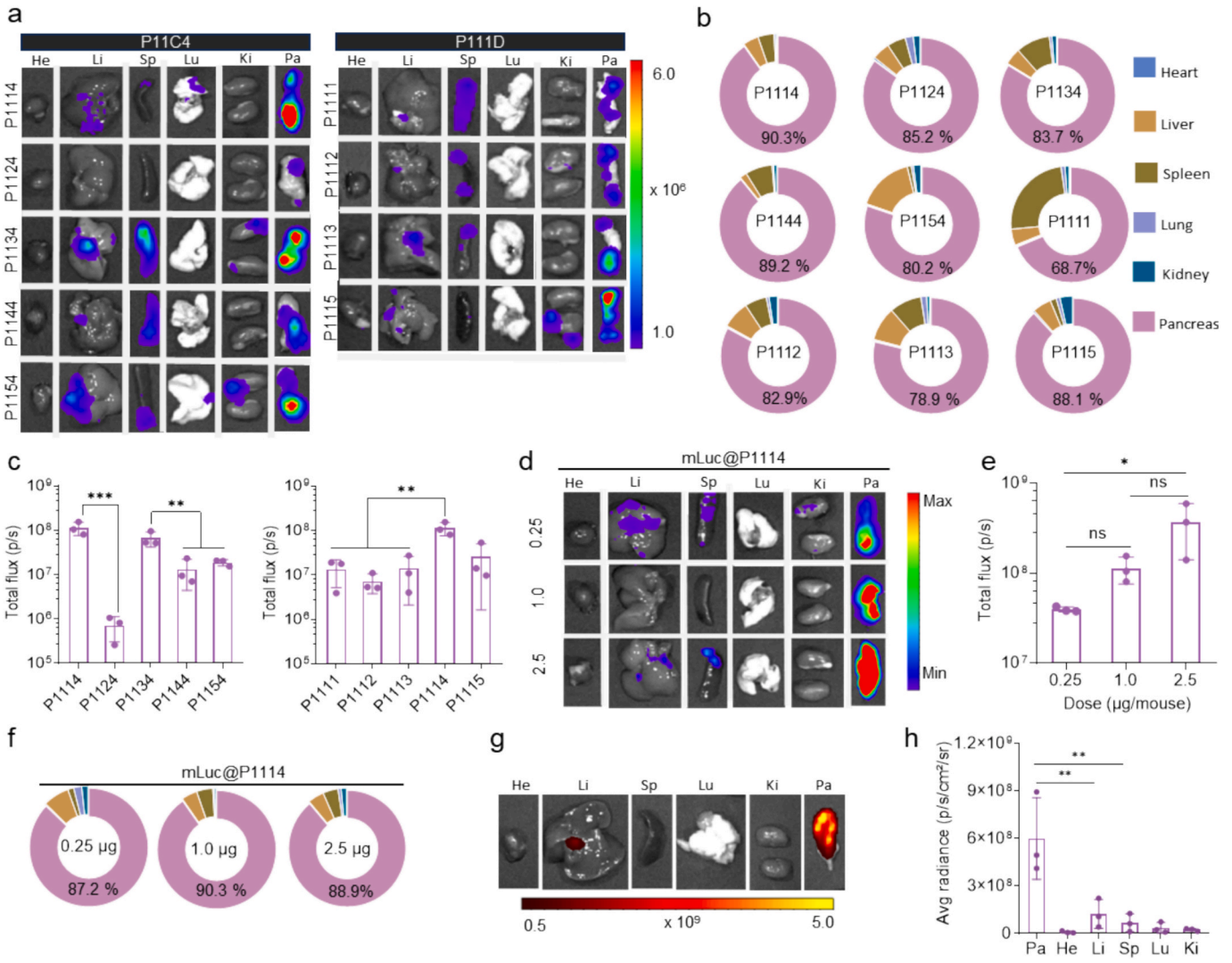

Fig. 4. In vivo screening of representative PAAs for pancreas transfection. (a-c) Screening of representative PAAs for mRNA delivery following intraperitoneal injection of mLuc@PAAs for 6 h (1.0 μg mLuc/mouse, n = 3). Representative luminescence images of major organs (a), percentage of luminescence intensity for each organ relative to the total luminescence across all organs (b), and quantification of luminescence intensity in the pancreas (c). (d-f) mRNA expression levels in the pancreas at various mRNA doses (0.25, 1.0, and 2.5 μg mLuc/mouse, n = 3) after intraperitoneal injection of mLuc@P1114 for 6 h. Representative luminescence images of major organs (d), quantification of luminescence intensity in the pancreas (e), and quantification of pancreatic luminescence intensity as a percentage of the total luminescence across all organs (f). (g-h) Biodistribution of mLuc-Cy5@P1114 following intraperitoneal injection for 6 h (n = 3). Representative fluorescence images of major organs (g), and quantification of fluorescence intensity across major organs (h). For (c), (e), and (h) statistical significance was analyzed by the two-tailed unpaired *t*-test. *$p < 0.05$; **$p < 0.01$; ***$p < 0.001$; ****$p < 0.0001$; ns, not significant.

We further evaluated the mRNA expression kinetics of mGFP@P1114 in HeLa cells. Notably, mGFP@P1114 achieved nearly 90% GFP^+ cells within 2 h, 2.9-fold higher than Lipo MessengerMAX and 3.7-fold higher than jetMESSENGER (Fig. 3**k and** Fig. S17). The proportion of GFP-positive cells in mGFP@P1114 group peaked at 4 h, whereas the increase in GFP-positive cells was more gradual and slower for Lipo MessengerMAX and jetMessenger, underscoring the efficiency of membrane fusion-mediated cytosolic delivery for accelerated therapeutic protein expression. Serum protein corona formation poses a significant challenge for cationic mRNA delivery systems. Although incubation of mRNA@P1114 nanocomplexes in 80% FBS led to gradual particle size enlargement due to protein adsorption (Fig. S13c), cellular uptake remained remarkably efficient, with over 96% of cells internalizing the nanocomplexes within 15 min, comparable to serum-free conditions (Fig. S18a, b). In addition, inhibition of multiple endocytic pathways had negligible impact on transfection efficiency (Fig. S18c, d), confirming that direct membrane fusion remains the dominant cellular entry mechanism. These findings suggests that the preserved transfection performance of mRNA@P1114 in 80% FBS is not due to the absence of protein corona formation but rather to a distinct and rapid membrane-fusion-mediated cellular entry mechanism.

In vivo low-dose and selective mRNA transfection

Encouraged by the promising in vitro transfection, we further evaluated the in vivo mRNA delivery performance using P11C4- and P111D-based nanocomplexes. Through intraperitoneal administration at a low dose (1.0 μg mLuc/mouse), most PAAs demonstrated striking pancreas selectivity ranging from 80% to 90% (Fig. 4**a, b**). Notably, P1114 achieved peak selectivity of 90.3%, significantly surpassing conventional lipid nanoparticles and existing polymeric vectors [41,42]. Consistent with in vitro observations, both ionizable amines and aliphatic aldehyde moieties in PAAs critically influenced in vivo transfection efficiency. Among P11C4 derivatives, P1114 and P1134 showed superior performance, while P1114 demonstrated the optimal overall efficacy in the P111D series (Fig. 4**c**). Strikingly, even at an ultralow dose of 0.25 μg/mouse, P1114 maintained robust pancreatic transfection capacity, yielding 4.1×10^7 photons/s bioluminescent flux with 87.2% selectivity (Fig. 4**d-f**). Biodistribution analysis of mLuc-Cy5@P1114 following intraperitoneal administration confirmed preferential pancreas accumulation (Fig. 4**g**). Quantitative fluorescence intensity revealed significantly higher Cy5 signals in pancreas compared to liver and other organs (Fig. 4**h**), verifying the pancreatic-targeted enrichment and transfection.

The immunosuppressive tumor microenvironment (TME) of pancreatic adenocarcinoma leads to low response rates to immunotherapy and impaired T cell priming [43,44]. Interleukin-12 (IL-12), a critical proinflammatory cytokine, exhibits potent antitumor effects by promoting the proliferation and activation of cytotoxic T lymphocytes [45,46]. Nevertheless, the clinical application of IL-12 therapy is hindered by its short half-life and insufficient local concentration within tumors or lymph nodes, especially for tissues like the pancreas that are not easily accessible for local administration [47–49]. Encouraged by the efficient transfection with exceptional pancreas-targetability of P1114-mediated mRNA delivery, we explored the therapeutic potential of delivering mIL-12 to the pancreas in orthotopic KPC tumor models (Fig. 5**a**). mIL-12@P1114 significantly suppressed the growth of orthotopic KPC tumors and substantially extended the survival time of mice, significantly outperforming mIL-12@LNP at the same dose of 2.5 μg per mouse (Fig. 5**b-d**). Furthermore, the mIL-12@P1114 group maintained a remarkable 50% survival rate with no recurrence observed even after 250 days, whereas complete mortality occurred in the mIL-12@LNP group. Notably, even at an ultralow dose of 0.25 μg per mouse, mIL-12@P1114 exhibited significant tumor inhibition, extending the median survival time (MST) to 44 days. Meanwhile, the absence of significant weight loss in mIL-12@P1114-treated mice underscores the safety profile (Fig. 5**e**).

To assess the potential immunogenicity and long-term safety of the mRNA@P1114, we conducted a comprehensive analysis following triple dosing in mice. The administration of mRNA@P1114 did not induce significant acute systemic inflammation, as evidenced by little change in serum concentration of pro-inflammatory cytokines IL-1β and TNF-α (Fig. S19a, b). Hematological analysis further confirmed the absence of chronic inflammatory responses, with immune cell counts remaining within normal ranges throughout the observation period (from 15 to 250 days post-treatment) (Fig. S19c, d). Histopathological examination of major organs (heart, liver, spleen, lungs, and kidneys) revealed healthy tissue architecture without signs of lesions or damage (Fig. S20), corroborating the favorable safety profile of the P1114 delivery system for repeated administration. Furthermore, long-term monitoring of cured mice over a 250-day period demonstrated normal blood glucose levels and insulin secretion (Fig. S21), confirming the absence of pancreatic functional impairment.

Macrophage-mediated pancreas selective transfection

To elucidate the pancreatic targeting mechanism, we initially assessed the interactions of mLuc-Cy5@P1114 with the cells in peritoneal cavity following intraperitoneal injection. Flow cytometry analysis revealed that nearly all macrophages in peritoneum internalized mLuc-Cy5@P1114 nanocomplexes with 97.5% of $Cy5^+$cells after intraperitoneal injection for 2 h, which was significantly higher than those observed in B cells (64.6%) and T cells (40.4%) (Fig. 6**a, b**). The preferential uptake by macrophages likely arises from their strong scavenging activity and unique membrane features that enable efficient initial docking and fusion events, rather than the intrinsic selective membrane fusion mechanism with the nanocomplexes [50]. Although T/B cells demonstrated evident uptake, administration of mLuc@P1114 to immunodeficient nude mice lacking functional T cells revealed comparable pancreatic luminescence with selectivity and intensity to immunocompetent C57BL/6 mice (Fig. 4**c and** Fig. S22), indicating that T cells are dispensable for pancreatic targeting. To validate macrophage involvement, clodronate liposomes were intraperitoneally administered to deplete peritoneal macrophages, reducing their proportion from 28.6% to 17.5% (Fig. 6**c**). The specificity of macrophage depletion was confirmed by in vitro assays, where submicron clodronate liposomes efficiently eliminated BMDMs, while exhibited minimal cytotoxicity toward Jurkat cells (Fig. S23). Subsequent mLuc@P1114 injection in macrophage-depleted mice resulted in markedly diminished pancreas transfection efficiency (Fig. 6**d, e**), strongly implicating macrophages as crucial mediators of pancreatic delivery. Furthermore, intraperitoneal administration of mLuc@P1114-transfected BMDMs resulted in strong and selective pancreatic bioluminescence (Fig. S24), demonstrating that macrophages alone are capable for targeted pancreatic delivery. This preferential macrophage uptake aligns with macrophage-mediated transport of lipoplexes and vesicles to target organs as previous reports [41,51]. Subsequently, GFP expression and macrophage infiltration in the pancreas were assessed after the intraperitoneal injection of mGFP@P1114. Immunofluorescence imaging demonstrated pronounced GFP expression in pancreatic draining lymph nodes (dLNs), with much less direct pancreas transfection (Fig. 6**f and g**). Notably, GFP signals were also detected in non-macrophage cells within pancreatic dLNs (Fig. 6**f**), suggesting a potential secondary transfection mechanism. The partial co-localization of CD11b and GFP markers in dLNs aligns with a model in which nanocomplexes are initially predominantly taken up by peritoneal macrophages, followed by dissemination to adjacent cells. In this proposed framework, macrophages migrating to dLNs post-intraperitoneal uptake may undergo direct transfection ($CD11b^+GFP^+$), whereas the GFP signals in $CD11b^-$ cells likely arise from macrophage-mediated cargo redistribution potentially via extracellular vesicles or exosomes, as reported previously [41,51]. Supporting this hypothesis, conditioned medium from mGFP@P1114-transfected

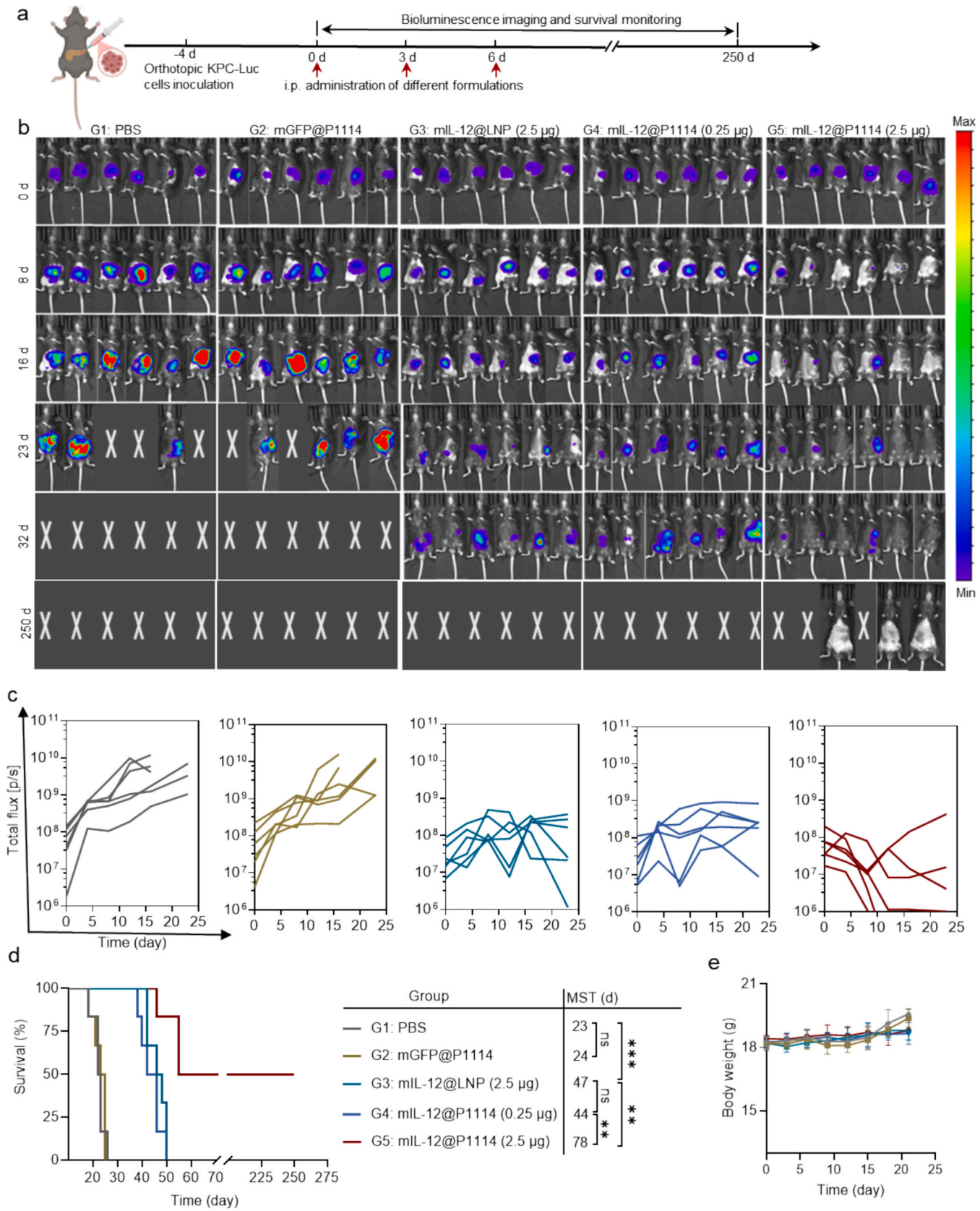

Fig. 5. Pancreas-targeted delivery of mIL-12 retards the growth of orthotopic pancreatic tumors. (a) Timeline for the treatment of orthotopic KPC tumor model. (b) In vivo luminescence images of mice at representative time points. (c) Individual luminescence intensities at different time points (n = 6). Survival curves (d) and body weight (e) of mice treated with different formulations (n = 6). Survival rate was analyzed by Kaplan-Meier technique with a log-rank (Mantel-Cox) test. $^{**}p < 0.01$; $^{***}p < 0.001$; ns, not significant.

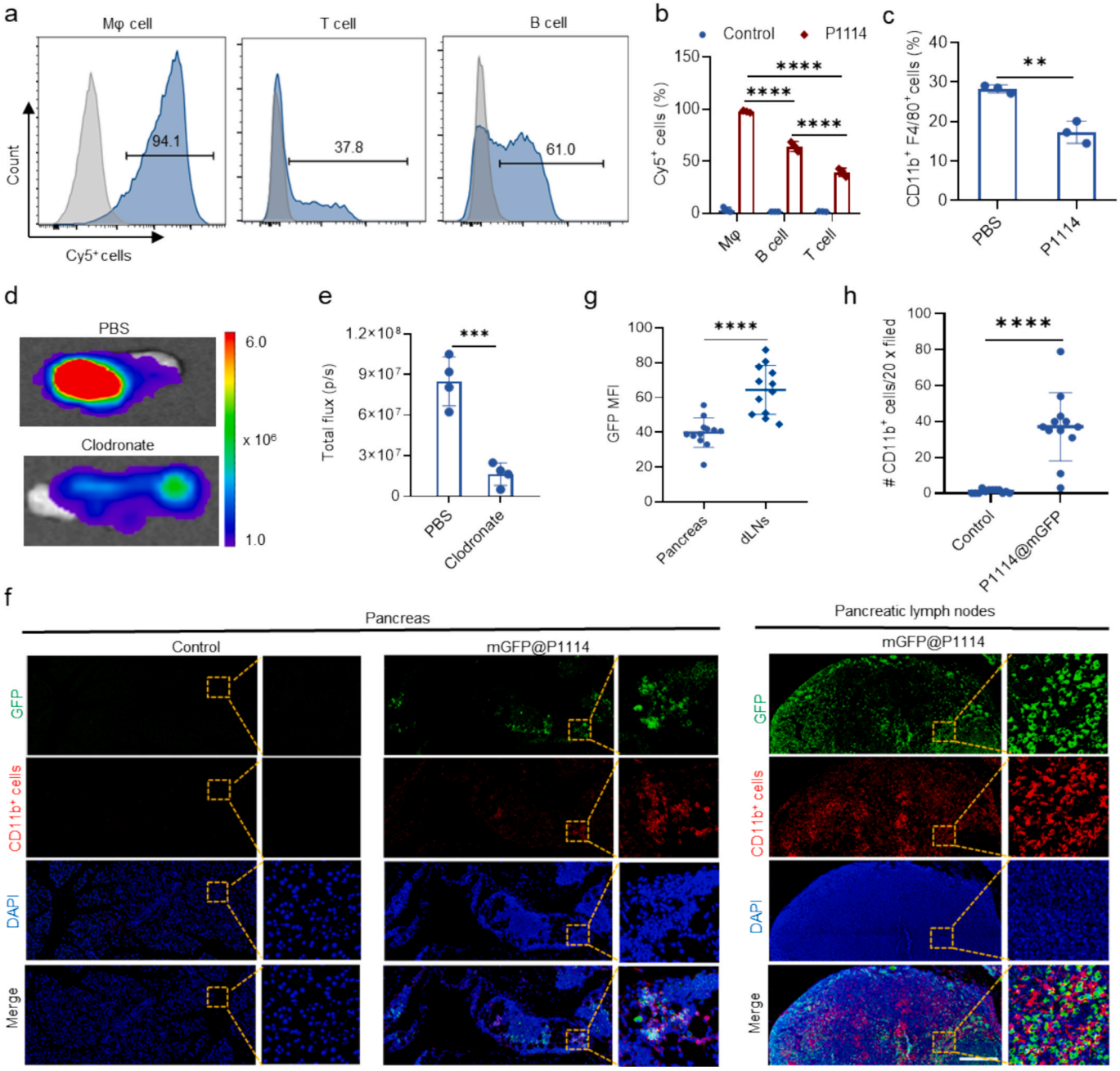

Fig. 6. Peritoneal macrophage-mediated selective transfection of pancreas. (a, b) Uptake of mLuc-Cy5@P1114 by T cells ($CD3^+$), B cells ($CD19^+$), and macrophages ($CD11b^+$ $F4/80^+$) in the peritoneal cavity 2 h post-intraperitoneal injection. (a) Representative flow cytometry analysis and (b) quantitative results (n = 3). (c) The ratio of peritoneal macrophages following intraperitoneal administration of clodronate liposomes. (d, e) mRNA expression in the pancreas after intraperitoneal injection of mLuc@P1114 for 6 h in mice treated with clodronate liposomes and PBS for 48 h. (f) Representative immunostaining images of CD11b and GFP in pancreas and pancreas's dLNs after intraperitoneal injection of mEGFP@P1114. Scale bar, 100 μm. (g) Quantification of mean GFP fluorescence intensity in pancreas and pancreas's dLNs (n = 3). (h) Quantification of $CD11b^+$ cells in pancreas (n = 3). All values are expressed as mean ± s.d. For (b), statistical significance was determined using ordinary one-way ANOVA with multiple comparisons. For (c), (e), (f), and (h), statistical significance was analyzed by the two-tailed unpaired *t*-test. $*p < 0.05$; $**p < 0.01$; $***p < 0.001$; $****p < 0.0001$; ns, not significant.

BMDMs induced GFP expression in Jurkat cells (Fig. S25), further implicating macrophage-mediated intercellular cargo transfer. Notably, mGFP@P1114 induced significant macrophage infiltration in the pancreas (Fig. 6**h**). These findings delineate a biphasic transport mechanism where peritoneal macrophages rapidly internalize mGFP@P1114 nanocomplexes, followed by preferential trafficking to pancreatic lymphoid tissue rather than parenchymal regions.

Discussion

The approval of COVID-19 mRNA vaccines has profoundly accelerated the evolution of mRNA therapeutic, which have been increasingly explored for the treatment of a multitude of diseases [1–3]. The clinical deployment of mRNA agents is still largely dependent on the innovation of effective delivery systems, with non-viral vectors based on LNPs or cationic polymers being particularly highlighted [5]. Nevertheless, following cellular internalization, the majority of nanoparticles are

prone to entrapment within endosomes, leading to low cytosol delivery efficiency (1–4%), which significantly diminishes mRNA bioavailability and thereby generally necessitates escalated dose to attain effective protein expression [14,15]. Regrettably, an excess of vectors and mRNA tends to accumulate within healthy tissues, potentially inciting inflammatory responses and cytotoxicity, particularly for non-biodegradable cationic polymers [52]. Membrane fusion represents a promising strategy for intracellular delivery, facilitating direct cytosolic mRNA delivery and bypassing endosomal entrapment, thereby significantly enhancing transfection efficiency and mRNA bioavailability [23,35].

We harnessed the Ugi four-component reaction to develop a library of PAAs, which are amenable to facile synthesis and structural modulation, thereby facilitating extensive screening for mRNA delivery [25]. Structure-activity relationships indicate that the structure of the aliphatic chains and tertiary amines exerts a significant influence on the mechanism of cytosolic mRNA delivery by PAAs. The optimized membrane-fusogenic PAA_{mef}, P1114, can directly deliver mRNA to the cytosol through membrane fusion, thereby circumventing endosomal entrapment and significantly enhancing mRNA utilization and transfection efficiency. P1114 demonstrated superb transfection performance across diverse cell types (immune cells, cancer cells, and healthy cells) at low doses (0.1–0.2 pg mRNA/cell), comparable to viral vectors. Most cationic polymers are prone to protein adsorption in serum environments, which hinders cellular uptake of the complexes and subsequent endosomal escape, thereby significantly diminishing transfection efficiency [35,36]. We observed that P1114 manifests remarkable serum resistance, sustaining membrane fusion-mediated transfection efficiency even in culture media with 80% FBS, markedly outperforming jetMessenger.

In vivo investigations have demonstrated that the P1114 achieves highly selective pancreatic accumulation and transfection following intraperitoneal administration, thereby significantly enhancing mRNA bioavailability while avoiding potential toxicity issues associated with non-selective distribution. The pancreatic-targeted delivery is not an inherent consequence of intraperitoneal administration, but is predominantly mediated by the intrinsic properties of P1114, which enable efficient macrophage uptake and productive transfection, thereby driving selective pancreatic enrichment. Crucially, the complexes can still achieve efficient pancreatic transfection even with intraperitoneal administration of mRNA at low dose, which significantly reduces the required amounts of vectors and mRNA while concurrently enhancing the feasibility of multiple repeated administrations. In the orthotopic KPC pancreatic cancer model, intraperitoneal administration of mIL-12@P1114 achieves pancreas-selective transfection, which significantly ameliorates the immunosuppressive tumor microenvironment and effectively suppresses tumor progression, with 50% of mice remaining tumor-free. Notably, the concomitant transfection of pancreatic tumors and pancreatic lymph nodes suggests a synergistic therapeutic mechanism, whereby intratumoral mIL-12 expression locally remodels the immunosuppressive microenvironment and enhances effector T cell and NK cell activity, while lymph node transfection promotes antigen presentation and primes tumor-specific T cells, collectively contributing to robust and durable antitumor immunity. The efficient macrophage internalization, lymphoid tissue targeting via transfected macrophage migration to pancreatic-draining lymph nodes, and spatially confined antigen expression and immune activation highlighted the strong vaccine potential of mRNA@P1114.

Conclusions

In summary, we have established a structurally diverse polyamidoamine library for mRNA delivery via the Ugi four-component reaction, providing an efficient platform for systematic synthesis and structural optimization. Structure-activity relationship studies reveal that aliphatic chain length and tertiary amines play pivotal roles in governing cytosolic mRNA delivery mechanisms. Through comprehensive screening, we have identified the membrane-fusogenic P1114 polymer, which enables direct cytosolic mRNA delivery via membrane fusion, bypassing conventional endosomal pathways. P1114 demonstrates superior transfection performance across multiple cell types, achieving viral vector-level efficiency (0.1–0.2 pg mRNA/cell) while maintaining robust transfection even in high serum environments up to 80%. Strikingly, intraperitoneal administration of P1114-formulated mRNA induces pancreas-selective accumulation and transfection via macrophage-mediated transport. Therapeutic application of low-dose mIL-12@P1114 significantly suppresses orthotopic KPC pancreatic tumor progression and extends survival beyond the clinical benchmark SM-102 lipid nanoparticles. Thus, the membrane-fusogenic PAAs achieve both ultralow-dose and organ-specific mRNA transfection, opening a new horizon for mRNA therapy.

CRediT authorship contribution statement

Xiaofei Zhao: Writing – original draft, Validation, Methodology, Investigation, Formal analysis, Data curation. **Qiongzhe Ren:** Writing – original draft, Validation, Methodology, Investigation, Formal analysis, Data curation. **Xin Wang:** Methodology, Investigation. **Siyu Wang:** Methodology, Investigation. **Congcong Xu:** Methodology, Investigation. **Zhiyuan Zhong:** Writing – review & editing, Project administration, Formal analysis, Conceptualization. **Chao Deng:** Writing – review & editing, Supervision, Project administration, Funding acquisition, Conceptualization.

Ethics approval and consent to participate

All animal experiments were approved by the Animal Care and Use Committee of Soochow University (P.R. China), and all protocols conformed to the Guide for the Care and Use of Laboratory Animals.

Declaration of competing interest

The authors declare that they have no known competing financial interests or personal relationships that could have appeared to influence the work reported in this paper.

Acknowledgments

This work was supported by the National Natural Science Foundation of China (52373299) and the National Key R&D Program of China (2022YFB3804600).

Appendix A. Supplementary data

Supplementary data to this article can be found online at https://doi.org/10.1016/j.mattod.2026.103352.

Data availability

Data will be made available on request.

References

[1] A.J. Barbier, et al., The clinical progress of mRNA vaccines and immunotherapies, Nat. Biotechnol. 40 (2022) 840–854, https://doi.org/10.1038/s41587-022-01294-2.
[2] C. Liu, et al., mRNA-based cancer therapeutics, Nat. Rev. Cancer 23 (2023) 526–543, https://doi.org/10.1038/s41568-023-00586-2.
[3] S. Qin, et al., mRNA-based therapeutics: Powerful and versatile tools to combat diseases, Signal Transduct. Target. Ther. 7 (2022) 166, https://doi.org/10.1038/s41392-022-01007-w.
[4] E. Rohner, et al., Unlocking the promise of mRNA therapeutics, Nat. Biotechnol. 40 (2022) 1586–1600, https://doi.org/10.1038/s41587-022-01491-z.
[5] X. Hou, et al., Lipid nanoparticles for mRNA delivery, Nat. Rev. Mater. 6 (2021) 1078–1094, https://doi.org/10.1038/s41578-021-00358-0.

[6] S.A. Dilliard, D.J. Siegwart, Passive, active and endogenous organ-targeted lipid and polymer nanoparticles for delivery of genetic drugs, Nat. Rev. Mater. 8 (2023) 282–300, https://doi.org/10.1038/s41578-022-00529-7.
[7] S. Chen, et al., Nanotechnology-based mRNA vaccines, Nat. Rev. Methods Primers 3 (2023) 63, https://doi.org/10.1038/s43586-023-00246-7.
[8] N. McCann, et al., Viral vector vaccines, Curr. Opin. Immunol. 77 (2022) 102210, https://doi.org/10.1016/j.coi.2022.102210.
[9] Y. Chen, et al., Efficient non-viral CAR-T cell generation via silicon-nanotube-mediated transfection, Mater. Today 63 (2023) 8–17, https://doi.org/10.1016/j.mattod.2023.02.009.
[10] A.Y. Jiang, et al., Combinatorial development of nebulized mRNA delivery formulations for the lungs, Nat. Nanotechnol. 19 (2023) 364–375, https://doi.org/10.1038/s41565-023-01548-3.
[11] X. Han, et al., An ionizable lipid toolbox for RNA delivery, Nat. Commun. 12 (2021) 7233, https://doi.org/10.1038/s41467-021-27493-0.
[12] S. Wei Hu, et al., Nanobiomaterial vectors for improving gene editing and gene therapy, Mater. Today 66 (2023) 114–136, https://doi.org/10.1016/j.mattod.2023.04.011.
[13] X. Zhao, et al., Multivalent ionizable lipid-polypeptides for tumor-confined mRNA transfection, Bioact. Mater. 46 (2025) 423–433, https://doi.org/10.1016/j.bioactmat.2024.12.032.
[14] S. Chatterjee, et al., Endosomal escape: A bottleneck for LNP-mediated therapeutics, Proc. Natl. Acad. Sci. U. S. A. 121 (2024) e2307800120, https://doi.org/10.1073/pnas.2307800120.
[15] P. Huang, et al., Cellular trafficking of nanotechnology-mediated mRNA delivery, Adv. Mater. 36 (2024) e2307822, https://doi.org/10.1002/adma.202307822.
[16] S.F. Dowdy, et al., Delivery of RNA therapeutics: The great endosomal escape!, Nucleic Acid Ther. 32 (2022) 361–368, https://doi.org/10.1089/nat.2022.0004.
[17] Y. Rui, et al., High-throughput and high-content bioassay enables tuning of polyester nanoparticles for cellular uptake, endosomal escape, and systemic in vivo delivery of mRNA, Sci. Adv. 8 (2022) eabk2855.
[18] S. Liu, et al., Membrane-destabilizing ionizable phospholipids for organ-selective mRNA delivery and CRISPR-Cas gene editing, Nat. Mater. 20 (2021) 701–710, https://doi.org/10.1038/s41563-020-00886-0.
[19] S. Liu, et al., Zwitterionic phospholipidation of cationic polymers facilitates systemic mRNA delivery to spleen and lymph nodes, J. Am. Chem. Soc. 143 (2021) 21321–21330, https://doi.org/10.1021/jacs.1c09822.
[20] Z. Zhang, et al., Dose-independent transfection of hydrophobized polyplexes, Adv. Mater. 33 (2021) e2102219, https://doi.org/10.1002/adma.202102219.
[21] J. Casper, et al., Polyethylenimine (PEI) in gene therapy: Current status and clinical applications, J. Control. Release 362 (2023) 667–691, https://doi.org/10.1016/j.jconrel.2023.09.001.
[22] A. Klipp, M. Burger, J.C. Leroux, Get out or die trying: Peptide- and protein-based endosomal escape of RNA therapeutics, Adv. Drug Deliv. Rev. 200 (2023) 115047, https://doi.org/10.1016/j.addr.2023.115047.
[23] Y. Zhuo, et al., Direct cytosolic delivery of siRNA via cell membrane fusion using cholesterol-enriched exosomes, Nat. Nanotechnol. 19 (2024) 1858–1868, https://doi.org/10.1038/s41565-024-01785-0.
[24] S. Omo-Lamai, Y. Wang, M. N. Patel, E. O. Essien, M. Shen, A. Majumdar, C. Espy, J. Wu, B. Channer, M. Tobin, S. Murali, T. E. Papp, R. Maheshwari, L. Wang, L. S. Chase, M. E. Zamora, M. L. Arral, O. A. Marcos-Contreras, J. W. Myerson, C. A. Hunter, A. Tsourkas, V. Muzykantov, I. Brodsky, S. Shin, K. A. Whitehead, P. Gaskill, D. Discher, H. Parhiz, J. S. Brenner, Lipid nanoparticle-associated inflammation is triggered by sensing of endosomal damage: Engineering endosomal escape without side effects, bioRxiv (2024). http://doi.org/10.1101/2024.04.16.589801.
[25] W. Dong, et al., Multicomponent synthesis of imidazole-based ionizable lipids for highly efficient and spleen-selective messenger RNA delivery, J. Am. Chem. Soc. 146 (2024) 15085–15095, https://doi.org/10.1021/jacs.4c00451.
[26] Y. Zhu, Y. Tao, Sequence-controlled and sequence-defined polypeptoidsviathe Ugi reaction: Synthesis and sequence-driven properties, Polym. Chem. 12 (2021) 4895–4902, https://doi.org/10.1039/d1py00658d.
[27] J. Renner, et al., Synthesis of ionizable lipids for gene delivery to the lung using an Ugi four component reaction, J. Am. Chem. Soc. 147 (2025) 17459–17467, https://doi.org/10.1021/jacs.5c04123.
[28] J. Chen, et al., Combinatorial design of ionizable lipid nanoparticles for muscle-selective mRNA delivery with minimized off- target effects, Proc. Natl. Acad. Sci. U. S. A. 120 (2023) e2309472120, https://doi.org/10.1073/pnas.
[29] E. Ben-Akiva, et al., Biodegradable lipophilic polymeric mRNA nanoparticles for ligand-free targeting of splenic dendritic cells for cancer vaccination, Proc. Natl. Acad. Sci. U.S.A. 120 (2023) e2301606120, https://doi.org/10.1073/pnas.2301606120.
[30] J. Shi, et al., Rational design of polymeric mRNA delivery vectors to achieve excellent room-temperature storage stability and delivery efficiency, Chem. Mater. 36 (2024) 5422–5435, https://doi.org/10.1021/acs.chemmater.4c00219.
[31] R. Moriguchi, K. Kogure, H. Harashima, Non-linear pharmacodynamics in the transfection efficiency of a non-viral gene delivery system, Int. J. Pharm. 363 (2008) 192–198, https://doi.org/10.1016/j.ijpharm.2008.07.020.
[32] R. Moriguchi, et al., Non-linear pharmacodynamics in a non-viral gene delivery system: Positive non-linear relationship between dose and transfection efficiency, J. Control. Release 110 (2006) 605–609, https://doi.org/10.1016/j.jconrel.2005.10.021.
[33] S. Thalmayr, et al., Molecular chameleon carriers for nucleic acid delivery: The sweet spot between lipoplexes and polyplexes, Adv. Mater. 35 (2023) e2211105, https://doi.org/10.1002/adma.202211105.
[34] W. McCormick, L.A. Mermel, The basic reproductive number and particle-to-plaque ratio: Comparison of these two parameters of viral infectivity, Virol. J. 18 (2021) 92, https://doi.org/10.1186/s12985-021-01566-4.
[35] H. Kong, et al., An antifouling membrane-fusogenic liposome for effective intracellular delivery in vivo, Nat. Commun. 15 (2024) 4267, https://doi.org/10.1038/s41467-024-46533-z.
[36] J. Lv, et al., A serum resistant polymer with exceptional endosomal escape and mRNA delivery efficacy for CRISPR gene therapy, Adv. Sci. 12 (2025) e2413006, https://doi.org/10.1002/advs.202413006.
[37] Z. Sun, et al., One-pot synthesis of dynamically cross-linked polymers for serum-resistant nucleic acid delivery, Biomater. Sci. 11 (2023) 5653–5662, https://doi.org/10.1039/d3bm00685a.
[38] Y. Zhang, et al., Opportunities and challenges for mRNA delivery nanoplatforms, J. Phys. Chem. Lett. 13 (2022) 1314–1322, https://doi.org/10.1021/acs.jpclett.1c03898.
[39] Y. Zhao, et al., Rational design of lipid nanoparticles: Overcoming physiological barriers for selective intracellular mRNA delivery, Curr. Opin. Chem. Biol. 81 (2024) 102499, https://doi.org/10.1016/j.cbpa.2024.102499.
[40] G. Wang, et al., Virus-mimetic DNA-ejecting polyplexes for efficient intracellular cancer gene delivery, Nano Today 39 (2021) 101215, https://doi.org/10.1016/j.nantod.2021.101215.
[41] J.R. Melamed, et al., Ionizable lipid nanoparticles deliver mRNA to pancreatic β cells via macrophage-mediated gene transfer, Sci. Adv. 9 (2023) eade1444, https://doi.org/10.1126/sciadv.ade1444.
[42] X. Guo, et al., A polymeric mRNA vaccine featuring enhanced site-specific mRNA delivery and inherent STING-stimulating performance for tumor immunotherapy, Adv. Mater. 37 (2025) e2410998, https://doi.org/10.1002/adma.202410998.
[43] N.A. Ullman, et al., Immunologic strategies in pancreatic cancer: Making cold tumors hot, J. Clin. Oncol. 40 (2022) 2789–2805, https://doi.org/10.1200/jco.21.02616.
[44] Z. Wan, et al., Overcoming pancreatic cancer immune resistance by codelivery of CCR2 antagonist using a STING-activating gemcitabine-based nanocarrier, Mater. Today 62 (2023) 33–50, https://doi.org/10.1016/j.mattod.2022.11.008.
[45] B. Mirlekar, Y. Pylayeva-Gupta, IL-12 family cytokines in cancer and immunotherapy, Cancers 13 (2021) 167, https://doi.org/10.3390/cancers13020167.
[46] J. Deckers, et al., Engineering cytokine therapeutics, Nat. Rev. Bioeng. 1 (2023) 286–303, https://doi.org/10.1038/s44222-023-00030-y.
[47] A.M. Nash, et al., Clinically translatable cytokine delivery platformfor eradication of intraperitoneal tumors, Sci. Adv. 8 (2022) eabm1032, https://doi.org/10.1126/sciadv.abm1032.
[48] B.N. Mills, et al., Stereotactic body radiation and interleukin-12 combination therapy eradicates pancreatic tumors by repolarizing the immune microenvironment, Cell Rep. 29 (2019) 406–421, https://doi.org/10.1016/j.celrep.2019.08.095.
[49] S.L. Hewitt, et al., Intratumoral IL12 mRNA therapy promotes TH1 transformation of the tumor microenvironment, Clin. Cancer Res. 26 (2020) 6284–6298, https://doi.org/10.1158/1078-0432.CCR-20-0472.
[50] L. Arrizabalaga, et al., Intraperitoneal administration of mRNA encoding interleukin-12 for immunotherapy in peritoneal carcinomatosis, J. Nanobiotechnol. 23 (2025) 113, https://doi.org/10.1186/s12951-025-03196-2.
[51] J. Liu, et al., Glypican-3-targeted macrophages delivering drug-loaded exosomes offer efficient cytotherapy in mouse models of solid tumours, Nat. Commun. 15 (2024) 8203, https://doi.org/10.1038/s41467-024-52500-5.
[52] D. Bitounis, et al., Strategies to reduce the risks of mRNA drug and vaccine toxicity, Nat. Rev. Drug Discovery 23 (2024) 281–300, https://doi.org/10.1038/s41573-023-00859-3.